

# Non-contact Atrial Fibrillation Detection from Face Videos by Learning Systolic Peaks

Zhaodong Sun, Juhani Junttila, Mikko Tulppo, Tapio Seppänen, and Xiaobai Li

**Abstract—Objective:** We propose a non-contact approach for atrial fibrillation (AF) detection from face videos. **Methods:** Face videos, electrocardiography (ECG), and contact photoplethysmography (PPG) from 100 healthy subjects and 100 AF patients are recorded. All the videos in the healthy group are labeled as healthy. Videos in the patient group are labeled as AF, sinus rhythm (SR), or atrial flutter (AFL) by cardiologists. We use the 3D convolutional neural network for remote PPG measurement and propose a novel loss function (Wasserstein distance) to use the timing of systolic peaks from contact PPG as the label for our model training. Then a set of heart rate variability (HRV) features are calculated from the inter-beat intervals, and a support vector machine (SVM) classifier is trained with HRV features. **Results:** Our proposed method can accurately extract systolic peaks from face videos for AF detection. The proposed method is trained with subject-independent 10-fold cross-validation with 30s video clips and tested on two tasks. 1) Classification of healthy versus AF: the accuracy, sensitivity, and specificity are 96.16%, 95.71%, and 96.23%. 2) Classification of SR versus AF: the accuracy, sensitivity, and specificity are 95.31%, 98.66%, and 91.11%. **Conclusion:** We achieve good performance of non-contact AF detection by learning systolic peaks. **Significance:** non-contact AF detection can be used for self-screening of AF symptom for susceptible populations at home, or self-monitoring of AF recurrence after treatment for the chronic patients.

**Index Terms—** Atrial Fibrillation (AF), Face Video, Remote Photoplethysmography (PPG), Wasserstein Distance, Systolic Peak

## I. INTRODUCTION

ATRIAL fibrillation (AF) is a common heart arrhythmia and about 2% of the global population is reported to have this disease [1]. AF might cause stroke and heart failure, but most of the AF episodes are asymptomatic in the early phase. Early detection of AF episodes is essential to avoid these severe diseases. The common method for AF diagnosis is to observe electrocardiography (ECG) signals measured from the electrodes attached on the chest. However, this requires

specific equipment to measure ECG signals and the diagnosis from ECG signals should be determined by cardiologists, which is not practical for daily check or long-term monitoring. Although some work in [2] designed automatic AF detection algorithms from ECG and achieve a high accuracy, the acquisition of ECG signals is still a problem and not convenient for daily use. The AF detection from ECG can be based on 1) P-wave detection [3] or 2) R-R interval variability [4], [5]. P waves are not prominent features and are often influenced by artifacts, while R peaks have higher amplitudes which can be easily detected. AF patients have a larger R-R interval variability, which means the cardiac rhythm of AF patients shows larger irregularity, so the features from R-R interval variability can be a good indicator for AF detection.

### A. Contact measurement for AF detection

Although ECG is a gold standard for AF diagnosis, some studies found contact photoplethysmography (PPG) [6], [7] measured from fingertips and ballistocardiograph (BCG) [7]–[9] can also be used for AF detection. PPG and BCG signals do not have the P-wave in ECG, so the systolic peaks in PPG and BCG are the only clue for AF detection. Similar to the R-peaks in ECG, the systolic peaks are also an indicator of cardiac rhythm and the peak-peak intervals can also be used to derive the heart rate variability (HRV) features. For the daily use and better accessibility, some work proposed to use the accelerometer and gyroscope of a smartphone on the chest to get the BCG signal for AF detection [10], while others proposed to use the camera of a smartphone [6] on the fingertips to get the contact PPG signals to detect AF. The AF detection from contact PPG and BCG provide other alternatives to ECG signals and is more convenient for daily health monitor. However, all of the ECG, BCG, and contact PPG methods require the sensors attached to the body/skin, which might cause irritation and hygiene issues. In addition, the specific biomedical equipment also decrease the accessibility of these methods to more populations

### B. Remote PPG for Non-contact AF detection

Recent studies [11], [12] showed that remote PPG from face videos captured by a camera can be used for non-contact AF detection. In addition, Some smart watch devices on the wrist can use contact ways to measure PPG/ECG for daily AF detection. [13] There are several situations where AF detection from face videos is preferred over smart watches. First, AF

Manuscript received on October 14, 2021; This study was supported by the Academy of Finland (project 323287 and 5326291) and the Finnish Work Environment Fund (Project 200414). *Corresponding author: Xiaobai Li.*

Zhaodong Sun, Tapio Seppänen, and Xiaobai Li are with the Center for Machine Vision and Signal Analysis, University of Oulu, FI-90014 Oulu, Finland (e-mail: zhaodong.sun@oulu.fi; tapio.seppanen@oulu.fi; xiaobai.li@oulu.fi).

Juhani Junttila, and Mikko Tulppo are with Research Unit of Internal Medicine, Medical Research Center Oulu, FI-90014 Oulu, Finland (e-mail: juhani.junttila@oulu.fi; mikko.tulppo@oulu.fi).

detection from face videos can be used for telemedicine during video conferences without specific medical instruments and can be accessible to more patients. Second, the contact measurement of smart watches is not applicable to some patients with skin burns or other skin diseases on the measurement locations. Third, cameras are ubiquitous and accessible such as in the smartphones or laptops, and much cheaper than the smart watches with ECG/PPG measurement. Finally, as smart phones are frequently used in our daily life, the AF detection from face videos can be integrated to smart phones for routine AF screening when unlocking with face recognition.

Remote PPG is measured from the face color change induced by the blood volume change [14]. As cameras are ubiquitous nowadays, this might lead to potential solutions or products for convenient AF screening. Similar to the contact PPG, remote PPG also has the systolic peaks [15] to derive the heart rate variability features. The problem is that remote PPG signals are subtle comparing to motion and illumination noises, and it is challenging to develop a method which can measure systolic peaks accurately enough for the task of AF detection.

Couderc et al. [11] first tried to do AF detection from face videos. They tested on a small dataset of 11 patients, and their method was basic. They averaged the face pixels in the green channel to get the remote PPG, and set threshold of one single HRV feature for AF detection. Their classification accuracy is not good enough for daily use, but their preliminary results indicated it is promising to do AF detection from face videos. Yan et al. [12] collected a dataset including 217 patients among which 75 patients showed AF. They used a pre-trained SVM with features from autocorrelation analysis and achieved 95.4% accuracy for the classification between AF patient vs. non-AF patients.

We released the first version of Oulu Bio-Face (OBF) dataset in [16], which includes 100 healthy subjects and six AF patients. A baseline method was tested and achieved an accuracy of 78.3% for AF detection. Yu et al. [17] later proposed a 3D convolutional neural network (3DCNN) for remote PPG measurement. The contact PPG signals were used as the reference with Pearson correlation as the loss function for training the model. The method was tested on OBF (the same dataset and same HRV features as in [16]) and achieved a higher accuracy of 80.22% for AF detection. Shi et al. [18] proposed a feature fusion approach by combining three remote PPG algorithms ([16], [19], [20]) for AF detection. The method was tested on the second version of OBF dataset including 30 prior-treatment AF patients and 100 healthy subjects, and achieved an accuracy of 92.56%.

### C. Limitations of Previous Non-contact AF Detection Studies

Previous methods [11], [12], [16]–[18] for non-contact AF detection have one or more of the following limitations. 1) Their AF detection accuracy is limited, as the systolic peak information was not exploited for training the remote PPG algorithms. Previous approaches (e.g., [17], [21], [22]) used the whole waveform of contact signals (i.e. contact PPG) as

the reference for training, which might be problematic as the waveform of remote PPG is not completely consistent with contact PPG [15]. Our method focuses on utilizing systolic peaks and the reasons are in two aspects. First, studies [6], [7], [11], [16]–[18] showed that HRV features computed using systolic peaks are sufficient for AF detection so the waveform is not needed. Second, the systolic peaks are the most prominent and reliable feature in remote PPG while other waveform features are subtle and easily contaminated by noises especially for AF patients with poor blood circulation. Directly using the systolic peaks for training might be a better solution. 2) Most of previous studies were tested on limited AF cases, and a larger scale of AF data is needed to make reliable evaluation of the methods. 3) The low diversity of datasets also limits their application scope. Previous studies mostly focused on classification of healthy person versus before-treatment AF patient. It is also important to compare before-treatment (AF) and after-treatment (sinus rhythm, SR) of the same patients, which was not concerned in any previous study yet. For example, [16]–[18] only used the prior-exercise healthy subjects and prior-treatment AF patients for AF detection. The healthy subjects after exercises were not included in their healthy group, which limits the range of heart rates. Although the dataset of [12] has 217 patients, their dataset does not have patients after cardioversion treatment and they only did the classification of AF patients vs. non-AF patients. Since their dataset does not have healthy subject, they also lack the classification between healthy subjects vs. AF. 4) Previous studies (except [16]) did not compare the remote AF detection performance with results from ECG or contact PPG. The AF detection results from ECG or contact PPG can be an performance upper bound from which we can see the gap between non-contact and contact AF detection. Although Yan et al. [12] included the AF detection results from contact PPG, their contact PPG is captured from a phone camera not from a pulse oximeter and the quality of contact PPG cannot be guaranteed, which is not enough to be the classification performance upper bound. In this work, we will mainly tackle the previous limitations of non-contact AF detection.

Our main contributions are listed below:

- We develop a deep learning-based remote PPG algorithm by using the timing of the systolic peaks as the ground truth and demonstrate that learning systolic peaks from face videos can facilitate non-contact AF detection.
- We record the full version of OBF dataset [16] for non-contact AF detection from face videos. The dataset contains videos from 100 healthy subjects and 100 AF patients. For each healthy subject, one video is recorded before exercises and another one is after exercises. For each AF patient, one video is before treatment and another one is after treatment. Each patient video is labeled as AF, SR, or atrial flutter (AFL) by cardiologists.
- We test two types of AF detection models for the self-screening of healthy subjects and patients, respectively, and achieve high accuracy. The classification between healthy subjects and patients with AF has the accuracy of 96.16%. The classification between patients with SR

and patients with AF has the accuracy of 95.31%.

## II. METHOD

In this section, we will introduce 3DCNN models for remote PPG measurement and how to train our model with the timing of systolic peaks to facilitate AF detection. We will also explain how to use the HRV features derived from systolic peaks for AF detection.

### A. Remote PPG measurement

1) *Preprocessing*: We first need to crop the face region from the face video. The face region is obtained from the landmarks generated from OpenFace [23]. We first get the minimum and maximum xy coordinates of the landmarks so that we can locate the face central point. The bounding box size is 1.2 time the range of y coordinate of landmarks and is fixed for each video. After getting the central point and the size of the bounding box, we can crop the face region from each frame as shown in Fig. 1. The cropped face is resized to  $128 \times 128$ .

2) *3DCNN for Remote PPG Measurement*: The cropped face is fed into 3-dimensional convolutional neural network (3DCNN) model [17] for remote PPG measurement. 3DCNN uses the 3D kernels to do the convolution on the video along the width, height, and time axis. We will use the similar 3DCNN architecture as [17] with one modification that will be illustrated in the next part. The model is shown in Fig. 2. The input for 3DCNN is the cropped face video clip  $x \in \mathbb{R}^{C \times H \times W \times T}$  where  $C$  is the number of color channels,  $H$  is the video height,  $W$  is the video width, and  $T$  is the video time length. The output remote PPG is  $p_r = G_\theta(x) \in \mathbb{R}^T$ . The input video is a 4D video signal while the network eliminates the height, width, and color dimensions and convert the 4D signal into a 1D remote PPG signal. To train this network, we need to minimize a loss function. The loss function is to measure the distance between the ground truth, which is the contact PPG  $p_c(t)$ , and the network output, which is the remote PPG  $p_r(t)$ . Previous method [17] used negative Pearson correlation as the loss function with the contact PPG as the ground truth. This loss function encourages the remote PPG signals and contact PPG signals have similar morphology. However, this loss function also encourages the model to learn some redundant information from the contact PPG such as diastolic peaks or some artifacts.

3) *Binary Systolic Peaks for 3DCNN Training*: Using contact PPG as the ground truth to train the network is not the best. The systolic peak timing in the contact PPG is a better ground truth. There are two reasons. First, [15] demonstrated that the waveform morphology of contact PPG signals are not completely consistent with remote PPG due to their difference measurement locations. This means that contact PPG is not the completely true ground truth for each face video due to the inconsistency of contact and remote PPG. However, they showed that the timing of systolic peaks is the consistent information between contact and remote PPG. Second, we observe that the contact PPG from patients with AF have more artifacts than that from healthy subjects as shown in Fig. 3. In addition, the contact PPG from patient also has some systolic

peaks with much lower amplitude. If we use the contact PPG as the ground truth for model training, the model might learn some redundant information and ignore some systolic peaks with low amplitude. Therefore, we will convert our contact PPG into binary systolic peaks as shown in Fig. 3. The binary systolic peaks only have zeros and ones, which means the it only keeps the timing of the systolic peaks and remove other redundant information. This kind of ground truth can encourage the model to only learn the timing of systolic peaks, which is also the only information used for AF detection.

The next question is how can we use the binary systolic peaks for our model training. We can regard our model output  $p_r = G_\theta(x)$  and our binary systolic peak label  $s$  as two probability distributions so that we can use some probability distribution distances as our loss function. The reason is that probability distribution distances are able to compare a binary pulse signal with a continuous smooth signal. Our systolic peak signal is just a series of binary signals and our model output is the continuous smooth signal, so probability distribution distances might be a good choice. Previous used negative Pearson correlation loss function can handle continuous values in contact PPG, but cannot work with binary values in binary systolic peak signals.

In order to satisfy the requirement of probability distributions, we should make sure that the sum of a signal is one and the signal is non-negative. We can normalize the binary systolic peak as  $\bar{s} = s / \sum_i s_i$ . Since the softmax layer can make sure the model output is non-negative and the sum is one, we add a softmax layer to the output of the network  $G_\theta(x)$  and the new network is  $H_\theta(x) = \text{softmax}(G_\theta(x))$ . The diagram and detailed description of our model is shown in Fig. 2. Therefore, we have our new model output  $\bar{p}_r = H_\theta(x)$ . Our new loss function  $l(\bar{s}, \bar{p}_r)$  is defined to measure the distance between normalized systolic peak signal  $\bar{s}$  and model output  $\bar{p}_r$ . We use Wasserstein distance as our loss function  $l$  for learning the systolic peaks. The full analysis about the loss function selection is described in the next section.

### B. AF detection with HRV features

The AF detection part is shown in the right part of Fig. 1. We use the findpeak function in Scipy library<sup>1</sup> to find the systolic peaks from the model output signal and obtain the inter-beat interval (IBI) curve. The inter-beat interval is the time interval between two consecutive systolic peaks. A series of HRV features can be calculated from the inter-beat interval. In previous studies [6], [7], [11], [16], [18], multiple HRV features were demonstrated to be effective for AF detection. We take these studies as references and selected 21 features as listed below. The features were used to train a SVM classifier with radial basis function (RBF) kernel for AF detection.

- Time domain: mean IBI, standard deviation of IBI (SDNN), standard deviation of successive difference of IBI (SDSD), percentage of samples with more than 50 ms difference from the consecutive beat (pNN50), percentage of samples with more than 20 ms difference from the

<sup>1</sup><https://docs.scipy.org/doc/scipy/index.html>

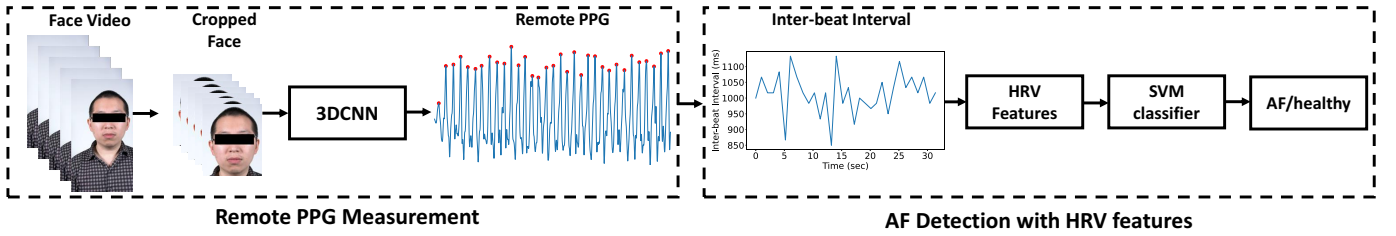


Fig. 1. The general framework of non-contact AF detection. The red dots in the remote PPG are the systolic peaks. Since this is a general framework, the remote PPG algorithm block can be a traditional remote PPG algorithms or a trained deep learning model.

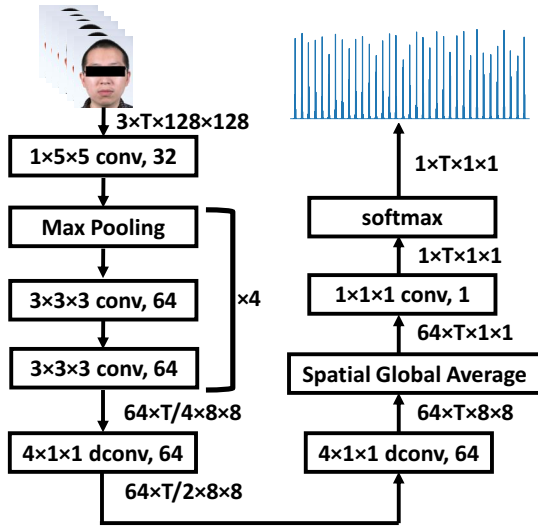


Fig. 2. 3DCNN architecture. The input is the image sequence of the cropped face. The output is the systolic peak signal. "3x3x3 Conv, 64" means the 3D convolution operation with filter size 3x3x3 and the output channel is 64. "dconv" is 3D transposed convolution, which works as upsampling. There is also a batchnorm layer and a ReLU activation following each convolutional block. There are 4 max pooling layer. all of them downsample the spatial dimensions and two of them only downsample the temporal dimension.

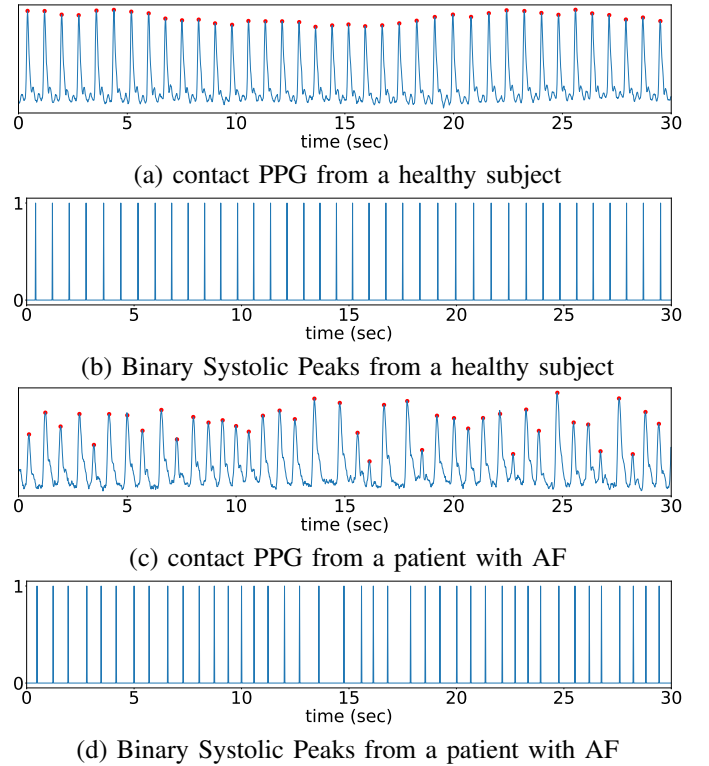


Fig. 3. Contact PPG (with systolic peaks marked with red dots) and binary systolic peaks from a healthy subject and a patient with AF. The binary systolic peaks are extracted from the corresponding contact PPG.

consecutive beat (pNN20), the number of samples with more than 50 ms difference from the consecutive beat (NN50), the number of samples with more than 20 ms difference from the consecutive beat (NN20), The root mean square of successive differences of IBI (RMSSD), median of IBI, range of IBI, the coefficient of variation of successive differences (CVSD), the coefficient of variation (CVNNI), mean heart rate, maximum heart rate, minimum heart rate, and the standard deviation of heart rate.

- Spectral domain: the power in the low frequency (LF) (0.04Hz-0.15Hz), the power in the high frequency (HF) (0.15Hz-0.4Hz), and the ratio of LF and HF.
- Geometrical domain: Poincaré plot standard deviations (SD1, SD2)

### III. LOSS FUNCTION SELECTION FOR LEARNING SYSTOLIC PEAKS

In this section, we describe how we select loss functions to let the 3DCNN model better learn the systolic peaks. We will first introduce several candidate loss functions, and then analyze their performance about learning peaks from

simulation experiments and real experiments. Finally, we will visualize how the chosen loss function helps the 3DCNN model to learn the systolic peaks.

#### A. Candidate loss functions

For the proposed 3DCNN model, both the model output signal  $\bar{p}_r$  and the normalized binary systolic peaks  $\bar{s}$  can be regarded as probability distributions. Therefore, we can use some probability distribution distances to measure the similarity between them. These probability distribution distances can be used as loss functions for the model training. During training, the loss function is minimized so that our model output signal is well aligned with the systolic peak signals. In previous work [24], probability distribution distances were used for comparing two time series in power spectral density (PSD) domain. However, the accurate representation of systolic peaks can only be in the time domain. Therefore, we directly use the probability distribution distances in the time domain.

There are some options of probability distribution distances such as squared Euclidean distance, Kullback-Leibler (KL) divergence, Jensen–Shannon (JS) divergence, and Wasserstein Distance.

1) *Squared Euclidean Distance (SED)*: Squared Euclidean distance is a straightforward way to compare two time series. It measures the Euclidean distance between two probability distributions. It is also widely used as a loss function for deep learning models. It is defined as

$$l_{SED}(\bar{p}_r, \bar{s}) = \|\bar{p}_r - \bar{s}\|_2^2 \quad (1)$$

2) *Kullback-Leibler (KL) Divergence*: The KL divergence is another probability distribution distance, which is widely used as the loss function in classification tasks. In the classification tasks, it measures the distance between the true classification distribution and the predicted classification distribution. KL divergence is defined as

$$l_{KL}(\bar{p}_r, \bar{s}) = \text{KL}(\bar{s} \parallel \bar{p}_r) = \sum_{t=1}^T \bar{s}(t) \log \left( \frac{\bar{s}(t)}{\bar{p}_r(t)} \right) \quad (2)$$

3) *Jensen–Shannon (JS) Divergence*: JS divergence is based on KL divergence. Compared with KL divergence, JS divergence is symmetric and bounded between 0 and 1. It is defined as

$$l_{JS}(\bar{p}_r, \bar{s}) = \frac{1}{2} \text{KL}(\bar{p}_r \parallel \frac{\bar{p}_r + \bar{s}}{2}) + \frac{1}{2} \text{KL}(\bar{s} \parallel \frac{\bar{p}_r + \bar{s}}{2}) \quad (3)$$

4) *Wasserstein Distance*: Wasserstein distance is based on optimal transport. It finds the minimum cost to move the mass of one probability distribution to turn the probability distribution into another. It is defined as

$$l_{WS}(\bar{p}_r, \bar{s}) = \min_{\pi \in \Pi(\bar{p}_r, \bar{s})} \mathbb{E}_{(x,y) \sim \pi} [\|x - y\|] \quad (4)$$

where  $\Pi(\bar{p}_r, \bar{s})$  is a set containing all joint probability distributions with marginal distribution  $\bar{p}_r$  and  $\bar{s}$ . Wasserstein distance finds the optimal transport plan  $\pi$  so that the movement cost is minimum. However, the formula above has a min operation and cannot be directly used as a loss function. Since our signals  $\bar{p}_r$  and  $\bar{s}$  are one-dimensional, the Wasserstein distance has a closed form in one-dimensional case as shown below.

$$l_{WS}(\bar{p}_r, \bar{s}) = \int_0^1 |F_{\bar{p}_r}^-(u) - F_{\bar{s}}^-(u)| du = \sum_{t=1}^T |F_{\bar{p}_r}(t) - F_{\bar{s}}(t)| \quad (5)$$

where  $F_{\bar{p}_r}$  is the cumulative sum of  $\bar{p}_r$ , which is also the cumulative distribution function.  $F_{\bar{p}_r}^-$  is the inverse of function  $F_{\bar{p}_r}$ . The Wasserstein distance used for the model training is the rightmost part of equation 5. Fig. 6 shows the interpretation of the loss function. To calculate the value of the Wasserstein distance between two signals, we first get the cumulative sum of each signal. In Fig. 6, the first column shows the systolic peak signal  $\bar{s}$  and the model output signal  $\bar{p}_r$ . The second column shows the corresponding cumulative sum  $F_{\bar{p}_r}$  and  $F_{\bar{s}}$ . The third column is the zoom-in version of the second column. From equation 5, the Wasserstein distance is the absolute difference between the two cumulative sum curves, as the gray area shown in the third column of Fig. 6.

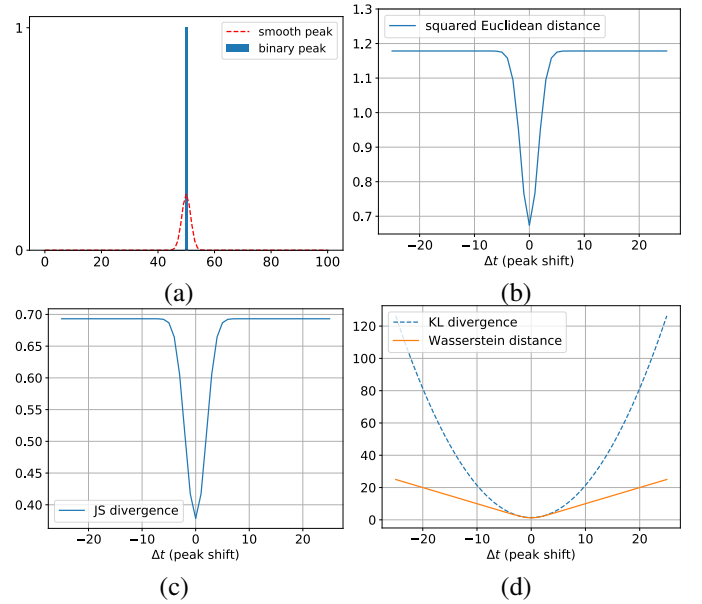


Fig. 4. (a) The smooth peak and binary peak. (b) Squared Euclidean Distance with respect to the peak shift  $\Delta t$ . (c) JS divergence with respect to the peak shift  $\Delta t$ . (d) KL divergence and Wasserstein distance with respect to the peak shift  $\Delta t$ .

## B. Analysis of Peak Misalignment

We first analyze the loss function response when two comparing signals are misaligned. We first generate a smooth peak signal  $p_s$  from a truncated Gaussian distribution curve  $\mathcal{N}(0, \sigma^2)$  with  $\sigma^2 = 0.1$  to imitate the 3DCNN model output and normalize it to make sure the sum is one. We also generate a binary peak signal  $p_b$  to imitate the ground truth systolic peak. These two signals are shown in Fig. 4(a). We shift the binary peak signal  $p_b(t)$  to  $p_{b,\Delta t}(t) = p_b(t - \Delta t)$  and get the loss function values  $l(p_s, p_{b,\Delta t})$ . We can plot the loss function values  $l(p_s, p_{b,\Delta t})$  with respect to peak shift  $\Delta t$  to see the loss functions response to the peak misalignment. The results are shown in Fig. 4(b-d). For squared Euclidean distance and JS divergence in Fig. 4(b-c), the loss value becomes saturated and constant when the absolute peak shift is too large, which means the loss function cannot assign larger penalty to larger peak alignment. This disadvantage might prevent the model to learn the accurate systolic peaks at these saturated locations. On the other side, KL divergence and Wasserstein distance in Fig. 4(d) will assign a larger penalty when the peak misalignment is larger and will not be saturated when the peak shift is large, which means KL divergence and Wasserstein distance could be the promising options.

## C. Analysis of Peak Sharpness

We also analyze the loss function response to peak sharpness. We hope the 3DCNN model to output signals with sharper peaks rather than flat ones, as sharper peaks are less impacted by noises and easier to be detected. We use the binary peak and a series of smooth peak signals with different variances  $\sigma^2$  to analyze the response of the loss function to the peak sharpness. We can change the variance  $\sigma^2$  of the truncated Gaussian distribution curve  $\mathcal{N}(0, \sigma^2)$  to control

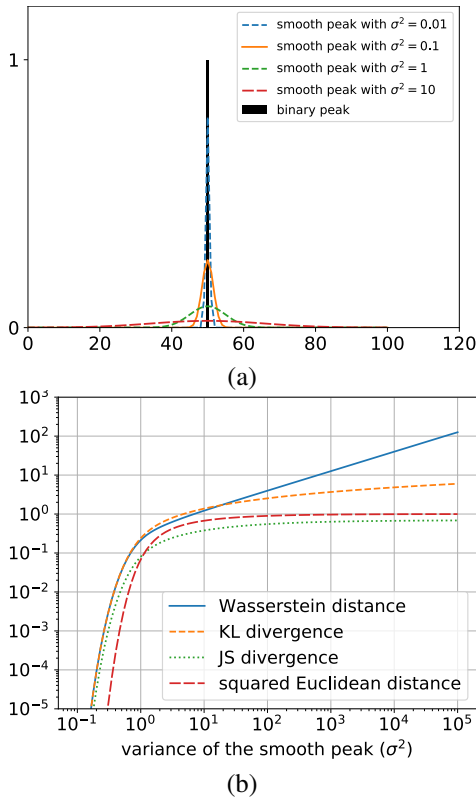


Fig. 5. (a) The binary peak and the smooth peak with difference variances (sharpness). (b) The loss values of the four candidate loss function with respect to the variance  $\sigma^2$  of the smooth peak.

the sharpness of the smooth peak  $p_{s,\sigma^2}$ . Smaller variance  $\sigma^2$  means sharper peaks. This phenomenon is illustrated in Fig. 5(a). The smooth peak with  $\sigma^2 = 10$  is almost flat while the the smooth peak with  $\sigma^2 = 0.01$  is very sharp and similar to the binary peak. By changing the variance  $\sigma^2$  of the smooth peak, we can plot the loss values  $l(p_{s,\sigma^2}, p_b)$  with respect to the variance  $\sigma^2$  of the smooth peak in Fig. 5(b). From the plot, Wasserstein distance has larger penalty values compared to other loss functions especially at large variance positions (small sharpness), which indicates Wasserstein distance can assign a much larger penalty value when the output peaks are too flat. Therefore, Wasserstein distance is the best to motivate the model to produce sharp peaks.

#### D. Experimental Validation

The above analysis based on our simulated binary and smooth single peak signals showed that the Wasserstein distance works best for training the 3DCNN model. In this part, we will directly use these four loss functions to train our model on actual dataset for learning systolic peaks. We use the whole OBF dataset for the model training with 10-fold cross validation. The full description of the OBF dataset will be presented in the next section. The numerical results about heart rate and IBI are shown in Table I. The metrics about IBI can indicate the accuracy of the systolic peaks. More details about these metrics are in the next section. From the experimental results, Wasserstein distance has the best performance in all metrics. Therefore, our experimental results

TABLE I

PERFORMANCE COMPARISON OF THE CANDIDATE LOSS FUNCTIONS

	Heart Rate (HR)			Inter-beat Interval (IBI)		
	MAE (bpm)	RMSE (bpm)	R	MAE (ms)	STD (ms)	Accuracy (%)
KL	8.77	16.45	0.51	189.44	435.86	83.84
JS	14.80	23.59	0.30	390.62	705.08	75.83
SED	7.18	14.39	0.58	159.77	437.77	86.07
WS	<b>1.46</b>	<b>3.53</b>	<b>0.96</b>	<b>50.74</b>	<b>68.06</b>	<b>94.18</b>

validate our analysis conclusion that Wasserstein distance is the best option.

#### E. Visualization about how Wasserstein Distance Boosts the Systolic Peaks

We plot the true systolic peaks and model output from one 30s video clip in the test set at epoch 1, 15, and 45 in Fig. 6 to show how Wasserstein distance boosts the predicted systolic peaks. The Wasserstein distance is the area between the two accumulative curves as shown in the second and third columns in Fig. 6. During model training, we intend to minimize this area so that the model output is similar to the systolic peak signal. Fig. 6 also shows the area between the two accumulative curves is decreasing as the training progresses. The decreasing of the area makes the peak signal from the model sharper and more accurately aligned with the true systolic peaks.

## IV. RESULTS AND DISCUSSION

In this section, we will first describe our OBF dataset with healthy subjects and AF patients. We will provide the experimental protocol, results, and discussion for our two experiments. One experiment is remote PPG measurement and another one is non-contact AF detection.

#### A. OBF Dataset

We record the full version of Oulu Bio-face (OBF) dataset with 100 healthy subjects and 100 AF patients. The healthy subjects were recruited from University of Oulu and AF patients were from Oulu University Hospital. The study was performed according to the Declaration of Helsinki, and the local committee of research ethics of the Northern Ostrobothnia Hospital District approved the protocol. The statistical information of participants is summarized in Table II. The partitions of healthy subjects and patients in OBF dataset are referred to as OBF-H and OBF-P, respectively. For each healthy subject in OBF-H, there are two 5-min videos. One video was recorded at a resting status and the other was recorded after 10 minutes exercise so that a wider range of heart rates are covered. For each patient in OBF-P, there are also two 5-min videos. One was recorded before cardioversion treatment (AF symptom presented) and the other was recorded after the treatment (back to sinus rhythm) so that each patient has both AF and SR data. The dataset structure and labels are

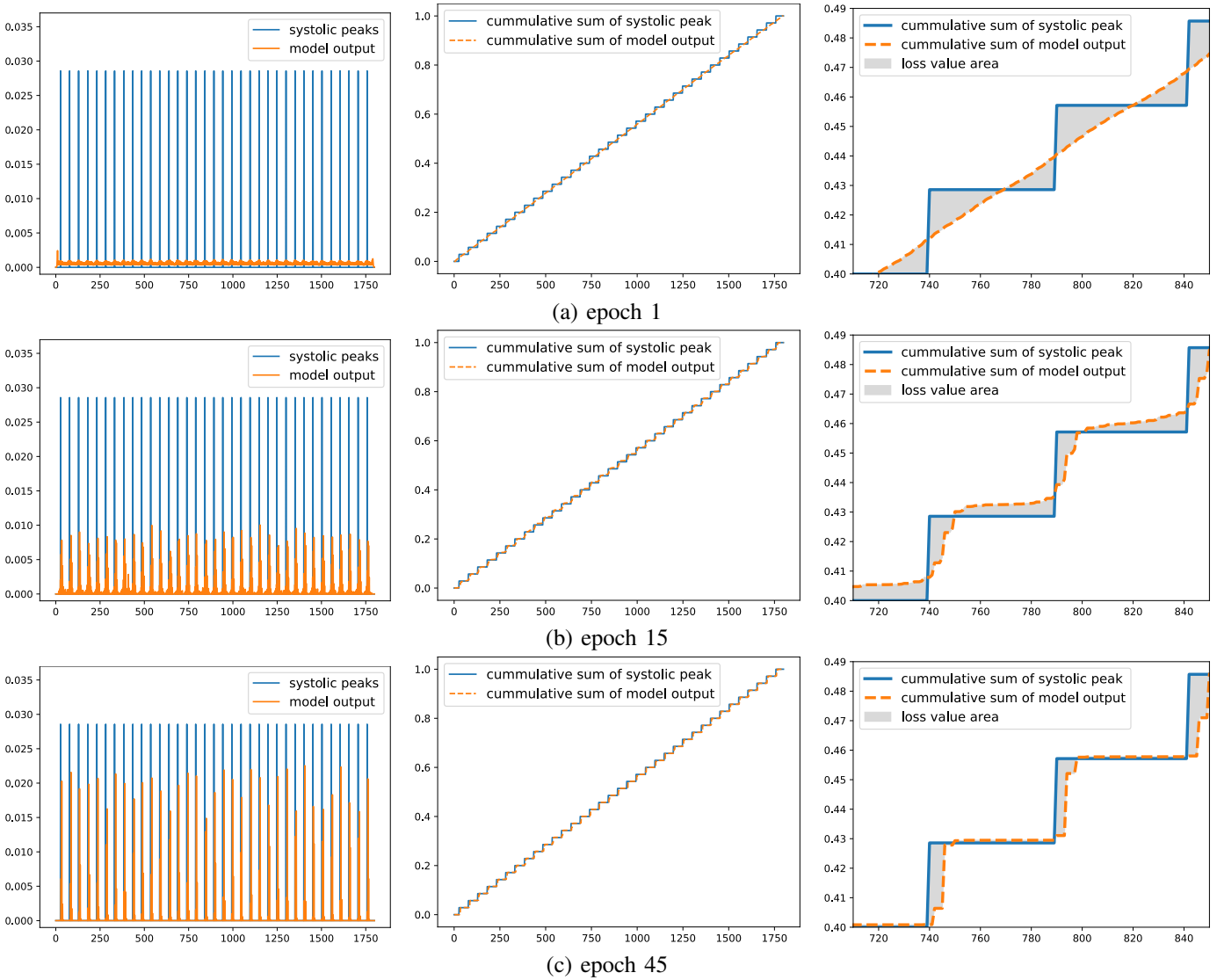


Fig. 6. Illustration of how Wasserstein distance boosts the predicted systolic peaks. The first ,second, and third row are at epoch 1, 15, and 45 of model training. The first column shows the ground truth systolic peaks and our model output. The second column shows the cumulative sum of the two signals in the first column. The third column is the zoom-in of the second column. The light gray area is the Wasserstein distance value.

shown in Fig. 7. The corresponding ECG and contact PPG were recorded simultaneously with each video clip. All of the videos are compressed by MPEG-4 with the resolution of  $1920 \times 1080$  and the frame rate of 60 fps. OBF-H has 200 videos. Due to data loss, some patients only have one session and the total number of videos in OBF-P is 169.

In order to do the AF detection, all the videos in OBF-H are labeled as healthy. All patients’ data in OBF-P were checked by two independent cardiologists by observing ECG signals. Finally, There are 73 videos labeled as AF, 61 videos labeled as SR, and 11 videos labeled as AFL. The remaining 24 videos were labeled as other (complex situation) and will not be used for classification. Similar to [13], we did not include the AFL group in our experiments due to limited AFL sample number.

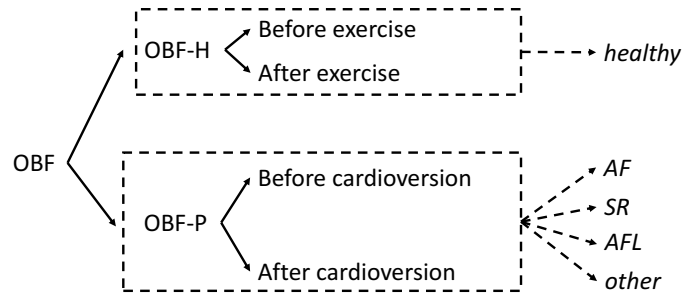


Fig. 7. OBF dataset structure and classification labels. OBF dataset has two partitions. OBF-H has the videos from healthy subjects before/after exercise. OBF-P has the videos from patients before/after cardioversion. All videos in OBF-H have the healthy label. Videos in OBF-P are labeled as AF, SR, AFL, or other by cardiologists.

**B. Experiment I: Remote PPG Measurement**

1) *Experimental Protocol*: We train our models with three dataset partitions, which are OBF-P, OBF-H, or the whole

OBF dataset. We also test our models on these three dataset partitions. The model is trained for 45 epochs with learning rate 0.0001. Each training video clip has 512 frames and

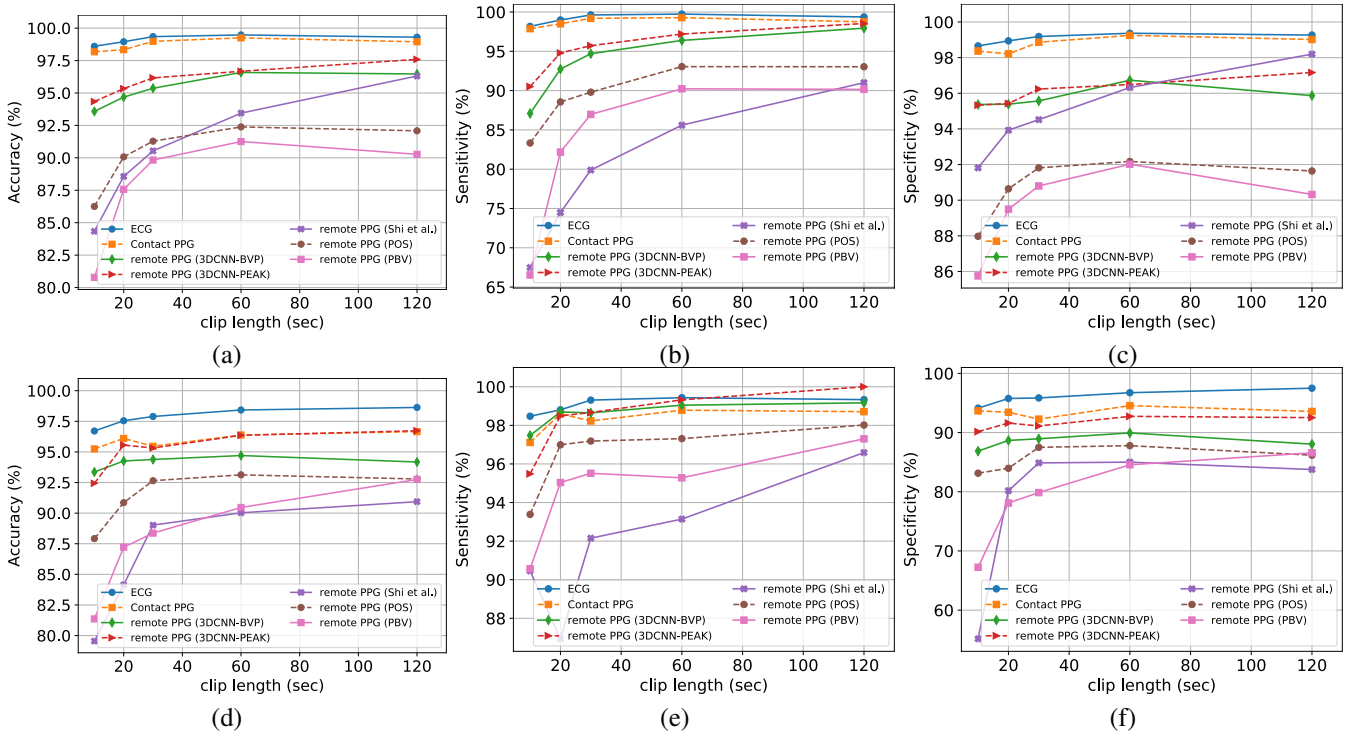


Fig. 8. (a-c) The accuracy, sensitivity, and specificity with respect to the clip length for AF vs. healthy. (d-f) The accuracy, sensitivity, and specificity with respect to the clip length for AF vs. SR.

TABLE II  
STATISTICAL INFORMATION OF THE PARTICIPANTS.

	Healthy (n=100)	Patient (n=100)
Age	31.6 ± 8.8, [18, 68]	64.2 ± 9.2, [43, 88]
Gender	61% M, 39% F	83% M, 17% F
Ethnic	Caucasian:32%, Asian:37%, Others:31%.	Caucasian: 100%
Weight (kg)	71 ± 16	96 ± 21
Ratio of wearing eyeglasses	39%	45%

the batch size for training is 4. The binary systolic peaks are obtained by NeuroKit2 [27] from our contact PPG and will be used as the ground truth to train the 3DCNN model. Wasserstein distance is used as the loss function with the binary systolic peaks. For testing, the videos are divided to non-overlapping 30-seconds clips and used as inputs. We use subject independent 10-folds cross validation in all experiments except two cases, i.e., training on OBF-H and testing on OBF-P, and training on OBF-P and testing on OBF-H, which use cross-set protocol. We also compare our method (3DCNN-PEAK) with four benchmark remote PPG methods: 3DCNN-BVP [17] is a deep learning-based method using whole contact PPG waveform for training. POS [19], CHROM [25], and PBV [26] are classical remote PPG algorithms without training.

2) *Evaluation Metrics*: We evaluate accuracy on two levels, i.e., the average heart rate level and IBI level. Accurate measure on the IBI level is more challenging and is essential for AF detection, as it requires accurate systolic peaks to compute

HRV features. We use mean absolute error (MAE), root mean squared error (RMSE), and Pearson correlation (R) to evaluate the error of the average heart rate of the testing clips. MAE for heart rate is defined as  $MAE_{HR} = \sum_{n=1}^N |HR_{video} - HR_{true}|/N$ , where N is the number of samples,  $HR_{video}$  is the heart rate measured from face videos, and  $HR_{true}$  is the true heart rate obtained from the contact PPG. RMSE is defined as  $RMSE_{HR} = \sqrt{\sum_{n=1}^N (HR_{video} - HR_{true})^2}/N$ . Small MAE and RMSE values indicate accurate heart rate estimation. Pearson correlation is the linear correlation between the heart rates measured from videos and the true heart rates. When the Pearson correlation is close to 1, the heart rate estimation is accurate.

We use three metrics of mean absolute error (MAE), standard deviation (STD), and accuracy as used in [28] to evaluate the error of IBI. We can first define the absolute error of IBI as  $AE = \sum_{t=1}^K |IBI_{video}(k) - IBI_{true}(k)|/K$  where K is the length of the IBI,  $IBI_{video}$  is the IBI curve from face video, and  $IBI_{true}$  is the true IBI curve from contact PPG. Since original IBI curve is an irregularly spaced time series, we should resample the original IBI curve to get the a evenly spaced time series so that we can calculate the the absolute error between 2 IBI curves. The MAE and STD of IBI is the mean and standard deviation of  $M_{IBI}$  for all samples. The accuracy of IBI is defined as  $AC_{IBI} = 1 - \frac{1}{N} \sum_{n=1}^N AE_n / (T / (B_n - 1))$  where T is the time length of a IBI curve and  $B_n$  is the number of systolic peaks in the  $n^{th}$  sample.

3) *Results and Discussion*: Table III shows the test results on OBF-P. No matter what training set is used, our proposed method 3DCNN-PEAK achieves the best performance on both heart rate (HR) and inter-beat interval (IBI). Using both OBF-



TABLE III  
RESULTS OF HEART RATE AND INTER-BEAT INTERVAL ON OBF-P

Training Set (Validation Protocol)	Remote PPG Algorithm	Heart Rate (HR)			Inter-beat Interval (IBI)		
		MAE (bpm)	RMSE (bpm)	R	MAE (ms)	STD (ms)	Accuracy (%)
OBF-P and OBF-H (10-folds)	3DCNN-PEAK	<b>2.5304</b>	<b>5.0275</b>	<b>0.9409</b>	<b>81.2244</b>	88.6318	<b>90.91</b>
	3DCNN-BVP [17]	3.7356	7.1297	0.8795	95.8779	122.6897	89.45
OBF-P (10-folds)	3DCNN-PEAK	3.3825	6.7187	0.8916	92.8611	99.0031	89.32
	3DCNN-BVP [17]	4.4277	8.3049	0.8350	104.1833	107.9021	88.21
OBF-H (cross dataset)	3DCNN-PEAK	3.6671	6.6110	0.8957	91.9969	<b>84.8351</b>	89.08
	3DCNN-BVP [17]	5.4465	9.9317	0.7562	109.1921	107.8691	86.68
-	POS [19]	6.2537	9.7026	0.7836	121.1604	93.5224	85.99
	CHROM [25]	7.2949	10.7810	0.7223	152.2947	90.2355	82.40
	PBV [26]	9.2961	13.0999	0.6294	159.7383	115.8414	82.28

TABLE IV  
RESULTS OF HEART RATE AND INTER-BEAT INTERVAL ON OBF-H

Training Set (Validation Protocol)	Remote PPG Algorithm	Heart Rate (HR)			Inter-beat Interval (IBI)		
		MAE (bpm)	RMSE (bpm)	R	MAE (ms)	STD (ms)	Accuracy (%)
OBF-P and OBF-H (10-folds)	3DCNN-PEAK	<b>0.4534</b>	<b>1.2868</b>	0.9954	<b>25.2568</b>	22.5873	<b>96.91</b>
	3DCNN-BVP [17]	0.7363	2.1517	0.9873	26.8545	25.6097	96.70
OBF-H (10-folds)	3DCNN-PEAK	0.5824	1.3059	<b>0.9955</b>	25.4702	<b>21.9592</b>	96.79
	3DCNN-BVP [17]	1.2912	3.4956	0.9676	33.1952	37.6494	95.78
OBF-P (cross dataset)	3DCNN-PEAK	1.2621	3.1478	0.9751	33.6131	29.8656	95.78
	3DCNN-BVP [17]	1.4451	4.3984	0.9447	39.4681	56.3431	95.16
-	POS [19]	2.1005	5.3898	0.9221	47.0708	50.3133	94.13
	CHROM [25]	4.1686	7.6021	0.8434	93.3947	51.5717	88.24
	PBV [26]	3.2652	6.2210	0.9106	63.8180	52.8818	92.24

P and OBF-H for training is more preferable since this can further improve the model performance compared with using OBF-P or OBF-H alone. The cross dataset test shown in the OBF-H row also indicates our 3DCNN-PEAK method has better generalization capability compared with 3DCNN-BVP method. Table IV shows the test results on OBF-H. Our 3DCNN-PEAK method still outperforms other baseline methods. It is obvious that the error of heart rate and IBI on OBF-H in Table IV is much lower than on OBF-P in Table III for all methods, which means the remote PPG measurement for patients is more difficult than for healthy subjects. We provide the final results of training and testing on the whole OBF dataset in Table V and our proposed 3DCNN-PEAK achieves the best results where MAE values of heart rate and IBI are 1.4658 BPM and 50.7481 ms, respectively.

### C. Experiment II: AF detection

1) *Experimental Protocol*: HRV features (as described in Section II.B) are calculated from the systolic peaks measured from face videos and used for AF detection experiments. We perform two kinds of AF detection. 1) We use videos from healthy subjects and videos with AF labels from patients to do the classification of healthy versus AF. 2) We use the patient videos with SR labels and patient videos with AF labels to do the classification of SR versus AF. We perform

the classification with different clip lengths of 10s, 20s, 30s, 60s, and 120s to see how the clip length influences the AF detection.

In all classification experiments, we use subject-independent 10-fold cross validation. We also report results achieved by using the ECG signals and contact PPG signals with the same HRV features and the same validation protocol as for the remotely measured PPGs. Theoretically, the ECG and contact PPG results should be the upper bound that the model can achieve. We also compare our results with four previous methods [17]–[19], [26].

2) *Evaluation Metrics*: AF detection results are summarized into true positive (TP), true negative (TN), false positive (FP), and false negative (FN). We use accuracy, sensitivity, and specificity as the classification metrics. Accuracy is defined as  $(TP + TN) / (TP + TN + FP + FN)$ , which evaluates the overall performance of the classification model. Sensitivity is defined as  $TP / (TP + FN)$ , which is the true positive rate. Specificity is defined as  $TN / (TN + FP)$ , which is the true negative rate. We also add metrics of F1 score and area under curve (AUC) for more convincing comparison.

3) *Results and Discussion*: Table VI and VII show the classification results for AF vs. healthy and AF vs. SR, respectively, when the clip length is 30s. For AF vs. healthy results in Table VI, two points can be observed. First, the

TABLE V  
RESULTS OF HEART RATE AND INTER-BEAT INTERVAL ON THE WHOLE OBF DATASET

	Heart Rate (HR)			Inter-beat Interval (IBI)		
	MAE (bpm)	RMSE (bpm)	R	MAE (ms)	STD (ms)	Accuracy
3DCNN-PEAK	<b>1.4658</b>	<b>3.5351</b>	<b>0.9686</b>	<b>50.7481</b>	<b>68.0636</b>	<b>94.18</b>
3DCNN-BVP [17]	2.1371	5.0769	0.9347	58.2923	91.6229	93.40
POS [19]	4.0234	7.6933	0.8568	81.3753	82.3035	90.36
CHROM [25]	5.6161	9.2114	0.7900	120.6662	77.8512	85.53
PBV [26]	6.0576	10.0119	0.7711	108.2304	100.0128	87.63

TABLE VI  
RESULTS OF CLASSIFICATION BETWEEN HEALTHY SUBJECTS AND PATIENTS WITH AF FOR 30s CLIPS

Signal Type	Measurement Method	Accuracy (%)	Sensitivity (%)	Specificity (%)	F1 (%)	AUC
ECG	ECG Sensor	99.34	99.62	99.18	98.99	0.9940
contact PPG	Pulse Oximeter	98.98	99.19	98.86	98.27	0.9903
remote PPG from face videos	3DCNN-PEAK	<b>96.16</b>	<b>95.71</b>	<b>96.23</b>	<b>92.98</b>	<b>0.9597</b>
	3DCNN-BVP [17]	95.36	94.69	95.56	91.72	0.9513
	Shi et al. [18]	90.53	79.88	94.51	81.96	0.8720
	POS [19]	91.28	89.80	91.81	85.27	0.9080
	PBV [26]	89.82	86.97	90.79	82.37	0.8888

TABLE VII  
RESULTS OF CLASSIFICATION BETWEEN PATIENTS WITH SR AND PATIENTS WITH AF FOR 30s CLIPS

Signal Type	Measurement Method	Accuracy (%)	Sensitivity (%)	Specificity (%)	F1 (%)	AUC
ECG	ECG Sensor	97.89	99.30	95.85	98.13	0.9757
contact PPG	Pulse Oximeter	95.46	98.22	92.27	96.06	0.9525
remote PPG from face videos	3DCNN-PEAK	<b>95.31</b>	<b>98.66</b>	<b>91.11</b>	<b>95.94</b>	<b>0.9489</b>
	3DCNN-BVP [17]	94.38	98.64	88.95	95.16	0.9380
	Shi et al. [18]	89.01	92.15	84.87	89.87	0.8851
	POS [19]	92.64	97.18	87.50	93.46	0.9234
	PBV [26]	88.36	95.51	79.86	89.93	0.8768

ECG and contact PPG both achieve high accuracy, which validates that the HRV features are effective for AF detection. Second, our proposed 3DCNN-PEAK achieves slightly lower performance than the contact PPG, but it works best among all remote PPG methods. The accuracy, sensitivity, and specificity for our method are 96.16%, 95.71%, and 96.23%, respectively, which is very close to the contact PPG results. For AF vs. SR results in Table VII, our method still achieves the best results among all remote PPG methods and the performance is very close to contact PPG. The accuracy, sensitivity, and specificity for our method are 95.31%, 98.66%, and 91.11%, respectively. Comparing the two tables, it can be seen that results of AF vs. SR are slightly lower than that of AF vs. healthy, which means the AF vs. SR classification task is more challenging. This is expected since both AF and SR samples are from the patients while the classification of AF vs. healthy uses data from two different groups of subjects that the data might be more heterogeneous. Besides, the contact PPGs from patients are more noisy than those from healthy subjects as shown in Fig. 3, let alone the remote PPGs. The noisy remote PPG from patients makes it more difficult to classify AF vs. SR.

Fig. 8 shows the accuracy, sensitivity, and specificity with

clip lengths of 10s, 20s, 30s, 60s, and 120s for both AF vs. healthy and AF vs. SR. In general, ECG has the best performance among all, and accuracy is high even with the shortest 10s clip length. Our proposed 3DCNN-PEAK outperforms other remote PPG methods at different clip lengths. We can also observe that longer clips can provide slightly better performance.

#### D. Computational Cost

We also evaluate the computational speed of each step of the proposed method as it is important to make the model feasible for real-time application usage. Our experiments were carried out on an Intel Xeon E5-2650 2.30 GHz CPU and Nvidia Tesla V100 GPU. The cropped face is first extracted from the original face videos by OpenFace [23]. The running speed of this step is 30 fps. We train our deep learning model with the whole OBF dataset (about 31 hours of face videos) for 45 epochs, which costs about 45 hours. The inference time of the model is about 2 ms ( $9 \times 10^5$  fps) to output the remote PPG curve for one 30s video clip. The training of SVM classification with 30s clips takes 60 ms. For each 30s clip, the inference time is about 1.2 ms ( $1.5 \times 10^6$  fps). The speed of

our remote PPG model and the SVM classification model have a very fast inference speed, which means it is very promising for real-time non-contact AF detection. The bottleneck of the whole framework is at the extraction of cropped face, which is beyond the scope of this work. The extraction of cropped face can be improved in future studies by using more advanced and fast landmark detection methods such as [29].

## V. CONCLUSION

In this paper, we propose a novel method for non-contact AF detection by utilizing the systolic peaks to train our deep learning model. Our method improves the performance of non-contact AF detection compared with other baselines. Our latest OBF dataset is also a comprehensive dataset for non-contact AF detection from face videos. From this dataset, we perform the classification of AF vs. healthy and AF vs. SR. The classification model for AF vs. healthy has the accuracy 96.16%, sensitivity 95.71%, and specificity 96.23%. The classification model for AF vs. SR has the accuracy 95.31%, sensitivity 98.66%, and specificity 91.11%.

Our results are promising that may lead to health-care products, e.g., for self-screening of AF symptom of susceptible populations at home, or self-monitoring for the chronic patients to check for recurrence of atrial fibrillation after treatment. Non-contact AF detection can also be used in public places for rapid screening of AF since this method does not need to take time to attach sensors to the subject. In addition, the non-contact way is more hygienic and does not take time to disinfect the sensor compared with contact ways. Non-contact AF detection can also be used for telemedicine during video conferences without specific medical instruments and can be accessible to more patients.

Our work currently focuses on AF detection from face videos. In the future work, we will try to use face videos to detect other cardiac rhythms such as AFL and extrasystoles. In addition, our current method is not end-to-end since the two modules including remote PPG measurement and AF detection with HRV features are not simultaneously trained. In the future work, the performance of non-contact AF detection can be improved by designing an end-to-end method.

## ACKNOWLEDGEMENTS

The authors thank Jingang Shi, Iman Alikhani, and Zitong Yu from University of Oulu for their important contributions in data collection. The authors wish to acknowledge CSC – IT Center for Science, Finland, for computational resources.

## REFERENCES

- [1] A. F. Members, A. J. Camm, G. Y. Lip, R. De Caterina, I. Savellieva, D. Atar, S. H. Hohnloser, G. Hindricks, P. Kirchhof, E. C. for Practice Guidelines (CPG), *et al.*, “2012 focused update of the esc guidelines for the management of atrial fibrillation: an update of the 2010 esc guidelines for the management of atrial fibrillation developed with the special contribution of the european heart rhythm association,” *European heart journal*, vol. 33, no. 21, pp. 2719–2747, 2012.
- [2] M. Butkuvienė, A. Petrenas, A. Solosenko, A. Martín-Yebra, V. Marozas, and L. Sornmo, “Considerations on performance evaluation of atrial fibrillation detectors,” *IEEE Transactions on Biomedical Engineering*, 2021.
- [3] M. Fukunami, T. Yamada, M. Ohmori, K. Kumagai, K. Umamoto, A. Sakai, N. Kondoh, T. Minamino, and N. Hoki, “Detection of patients at risk for paroxysmal atrial fibrillation during sinus rhythm by p wave-triggered signal-averaged electrocardiogram,” *Circulation*, vol. 83, no. 1, pp. 162–169, 1991.
- [4] K. Tateno and L. Glass, “Automatic detection of atrial fibrillation using the coefficient of variation and density histograms of rr and  $\delta rr$  intervals,” *Medical and Biological Engineering and Computing*, vol. 39, no. 6, pp. 664–671, 2001.
- [5] S. Dash, K. Chon, S. Lu, and E. Raeder, “Automatic real time detection of atrial fibrillation,” *Annals of biomedical engineering*, vol. 37, no. 9, pp. 1701–1709, 2009.
- [6] J. Lee, B. A. Reyes, D. D. McManus, O. Maitas, and K. H. Chon, “Atrial fibrillation detection using an iphone 4s,” *IEEE Transactions on Biomedical Engineering*, vol. 60, no. 1, pp. 203–206, 2012.
- [7] L. M. Eerikäinen, A. G. Bonomi, F. Schipper, L. R. Dekker, H. M. de Morree, R. Vullings, and R. M. Aarts, “Detecting atrial fibrillation and atrial flutter in daily life using photoplethysmography data,” *IEEE journal of biomedical and health informatics*, vol. 24, no. 6, pp. 1610–1618, 2019.
- [8] C. Bruser, J. Diesel, M. D. Zink, S. Winter, P. Schauerte, and S. Leonhardt, “Automatic detection of atrial fibrillation in cardiac vibration signals,” *IEEE journal of biomedical and health informatics*, vol. 17, no. 1, pp. 162–171, 2012.
- [9] T. Hurnanen, E. Lehtonen, M. J. Tadi, T. Kuusela, T. Kiviniemi, A. Saraste, T. Vasankari, J. Airaksinen, T. Koivisto, and M. Pänkäälä, “Automated detection of atrial fibrillation based on time–frequency analysis of seismocardiograms,” *IEEE journal of biomedical and health informatics*, vol. 21, no. 5, pp. 1233–1241, 2016.
- [10] O. Lahdenoja, T. Hurnanen, Z. Iftikhar, S. Nieminen, T. Knuutila, A. Saraste, T. Kiviniemi, T. Vasankari, J. Airaksinen, M. Pänkäälä, *et al.*, “Atrial fibrillation detection via accelerometer and gyroscope of a smartphone,” *IEEE Journal of Biomedical and Health Informatics*, vol. 22, no. 1, pp. 108–118, 2017.
- [11] J.-P. Couderc, S. Kyal, L. K. Mestha, B. Xu, D. R. Peterson, X. Xia, and B. Hall, “Detection of atrial fibrillation using contactless facial video monitoring,” *Heart Rhythm*, vol. 12, no. 1, pp. 195–201, 2015.
- [12] B. P. Yan, W. H. Lai, C. K. Chan, S. C.-H. Chan, L.-H. Chan, K.-M. Lam, H.-W. Lau, C.-M. Ng, L.-Y. Tai, K.-W. Yip, *et al.*, “Contact-free screening of atrial fibrillation by a smartphone using facial pulsatile photoplethysmographic signals,” *Journal of the American Heart Association*, vol. 7, no. 8, p. e008585, 2018.
- [13] A. G. Bonomi, F. Schipper, L. M. Eerikäinen, J. Margarito, R. Van Dinther, G. Muesch, H. M. De Morree, R. M. Aarts, S. Babaeizadeh, D. D. McManus, *et al.*, “Atrial fibrillation detection using a novel cardiac ambulatory monitor based on photo-plethysmography at the wrist,” *Journal of the American Heart Association*, vol. 7, no. 15, p. e009351, 2018.
- [14] W. Verkruyse, L. O. Svaasand, and J. S. Nelson, “Remote plethysmographic imaging using ambient light,” *Optics express*, vol. 16, no. 26, pp. 21434–21445, 2008.
- [15] D. McDuff, S. Gontarek, and R. W. Picard, “Remote detection of photoplethysmographic systolic and diastolic peaks using a digital camera,” *IEEE Transactions on Biomedical Engineering*, vol. 61, no. 12, pp. 2948–2954, 2014.
- [16] X. Li, I. Alikhani, J. Shi, T. Seppanen, J. Junttila, K. Majamaa-Voltti, M. Tulppo, and G. Zhao, “The obf database: A large face video database for remote physiological signal measurement and atrial fibrillation detection,” in *2018 13th IEEE International Conference on Automatic Face & Gesture Recognition (FG 2018)*, pp. 242–249, IEEE, 2018.
- [17] Z. Yu, X. Li, and G. Zhao, “Remote photoplethysmograph signal measurement from facial videos using spatio-temporal networks,” in *30th British Machine Vision Conference 2019, BMVC 2019, Cardiff, UK, September 9-12, 2019*, p. 277, BMVA Press, 2019.
- [18] J. Shi, I. Alikhani, X. Li, Z. Yu, T. Seppänen, and G. Zhao, “Atrial fibrillation detection from face videos by fusing subtle variations,” *IEEE Transactions on Circuits and Systems for Video Technology*, vol. 30, no. 8, pp. 2781–2795, 2019.
- [19] W. Wang, A. C. den Brinker, S. Stuijk, and G. De Haan, “Algorithmic principles of remote ppg,” *IEEE Transactions on Biomedical Engineering*, vol. 64, no. 7, pp. 1479–1491, 2016.
- [20] L. Feng, L.-M. Po, X. Xu, Y. Li, and R. Ma, “Motion-resistant remote imaging photoplethysmography based on the optical properties of skin,” *IEEE Transactions on Circuits and Systems for Video Technology*, vol. 25, no. 5, pp. 879–891, 2014.

- [21] Z. Yu, W. Peng, X. Li, X. Hong, and G. Zhao, "Remote heart rate measurement from highly compressed facial videos: an end-to-end deep learning solution with video enhancement," in *Proceedings of the IEEE/CVF International Conference on Computer Vision*, pp. 151–160, 2019.
- [22] X. Niu, Z. Yu, H. Han, X. Li, S. Shan, and G. Zhao, "Video-based remote physiological measurement via cross-verified feature disentangling," in *European Conference on Computer Vision*, pp. 295–310, Springer, 2020.
- [23] T. Baltrusaitis, A. Zadeh, Y. C. Lim, and L.-P. Morency, "Openface 2.0: Facial behavior analysis toolkit," in *2018 13th IEEE international conference on automatic face & gesture recognition (FG 2018)*, pp. 59–66, IEEE, 2018.
- [24] E. Cazelles, A. Robert, and F. Tobar, "The wasserstein-fourier distance for stationary time series," *IEEE Transactions on Signal Processing*, vol. 69, pp. 709–721, 2020.
- [25] G. De Haan and V. Jeanne, "Robust pulse rate from chrominance-based rppg," *IEEE Transactions on Biomedical Engineering*, vol. 60, no. 10, pp. 2878–2886, 2013.
- [26] G. De Haan and A. Van Leest, "Improved motion robustness of remote-ppg by using the blood volume pulse signature," *Physiological measurement*, vol. 35, no. 9, p. 1913, 2014.
- [27] D. Makowski, T. Pham, Z. J. Lau, J. C. Brammer, F. Lespinasse, H. Pham, C. Schölzel, and S. A. Chen, "Neurokit2: A python toolbox for neurophysiological signal processing," *Behavior Research Methods*, pp. 1–8, 2021.
- [28] X. Liu, X. Yang, J. Jin, and A. Wong, "Detecting pulse wave from unstable facial videos recorded from consumer-level cameras: A disturbance-adaptive orthogonal matching pursuit," *IEEE Transactions on Biomedical Engineering*, vol. 67, no. 12, pp. 3352–3362, 2020.
- [29] Y. Wu and Q. Ji, "Facial landmark detection: A literature survey," *International Journal of Computer Vision*, vol. 127, no. 2, pp. 115–142, 2019.